JGR Oceans

RESEARCH ARTICLE
10.1029/2019JC015436

Key Points:
- Topographic Rossby waves with an ~35-hr period were observed on the shelf break of the Chukchi Sea
- Key wave features included bottom-intensified fluctuations and significant coherence between near bottom temperature and upslope velocity
- Topographic Rossby wave events were found to coincide with strong wind-stress events, suggesting that they are triggered by wind forcing

Correspondence to:
J.-H. Park,
jaehunpark@inha.ac.kr

Citation:
Ku, A., Seung, Y. H., Jeon, C., Choi, Y., Yoshizawa, E., Shimada, K., et al. (2020). Observation of bottom-trapped topographic Rossby waves on the shelf break of the Chukchi Sea. *Journal of Geophysical Research: Oceans*, *125*, e2019JC015436. https://doi.org/10.1029/2019JC015436

Received 3 JUL 2019
Accepted 4 JUN 2020
Accepted article online 10 JUN 2020

©2020. American Geophysical Union. All Rights Reserved.

Observation of Bottom-Trapped Topographic Rossby Waves on the Shelf Break of the Chukchi Sea

Ahyoung Ku[1], Young Ho Seung[2], Chanhyung Jeon[3], Youngseok Choi[1,2], Eri Yoshizawa[4], Koji Shimada[5], Kyoung-Ho Cho[4], and Jae-Hun Park[6]

[1]Department of Marine Science and Biological Engineering, Inha University, Incheon, South Korea, [2]GeoSystem Research Corporation, Gunpo, South Korea, [3]Department of Mechanical Engineering, Massachusetts Institute of Technology, Cambridge, MA, USA, [4]Korea Polar Research Institute, Incheon, South Korea, [5]Department of Ocean Sciences, Tokyo University of Marine Science and Technology, Tokyo, Japan, [6]Department of Ocean Sciences, Inha University, Incheon, South Korea

Abstract This study investigates topographic Rossby waves (TRWs) with a period of approximately 35 hr using a mooring observation at 194-m depth on the shelf break of the Chukchi Sea in the Arctic Ocean. We measured velocity, temperature, and salinity for about 1 year from August 2014 to August 2015. The observations reveal that the bottom-intensified upslope current fluctuations were significantly coherent with near-bottom temperature fluctuations, with a phase lag of approximately 90°. Near the seafloor, the temperature increased with depth. Therefore, the temperature increases (decreases) with the upslope (downslope) currents. Theoretical estimates of the wavelength, angle of wavenumber vector, and bottom-trapping depth confirmed that the observed near 35-hr TRWs are indeed plausible in the study area. Energetic TRWs were observed in September and October, during the sea ice free season, whereas weak TRWs were observed in months with sea ice cover. The TRW events coincided with local wind-stress events, suggesting that the TRWs were triggered by atmospheric forcing. These findings imply that a longer ice-free season may allow for a more frequent occurrence of energetic TRWs, which may enhance the water exchange between the shallow continental shelf and the deep ocean.

Plain Language Summary A year-long time series of velocity and temperature showed fluctuations occurring every 35 hr in a shelf region of the western Arctic Ocean, located downstream of where Pacific Water flows into the Arctic through Bering Strait. Fluctuations were the strongest near the seabed on the shelf. Temperature fluctuations were found to be caused by vertical displacements of about 40 m of water parcels on the sloping topography. These features were consistent with topographic Rossby waves (TRWs), which are waves affected by bottom slope and stratification effects over sloping seabed. We used theoretical models to estimate wavelength and propagation angle using the local bottom slope and stratification. We also found that TRW events coincided with strong wind-stress events and were strong during the sea ice-free season and weak during the sea ice-covered season. These findings imply that a longer ice-free season may allow for a more frequent occurrence of wind-generated energetic TRWs, and this may lead to environmental changes in the shelf regions of the western Arctic Ocean.

1. Introduction

Pacific waters enter the Chukchi Sea via complex pathways (Corlett & Pickart, 2017) by flowing broadly to the Central Arctic (Woodgate, 2013) and making several detours to the Canada Basin (Shimada et al., 2005; Figure 1). In the shelf break of the Chukchi Sea, the slope current flows westward from the Chukchi slope, located in southern part of the Canada Basin. In the north of the slope current, in the southern part of the Chukchi Plateau, eddies pass sporadically (Corlett & Pickart, 2017). Around the Mendeleev Ridge and Chukchi Abyssal Plain, boundary currents flow eastward along the topography from the northwest Chukchi Sea to the east to the Canada basin (Woodgate et al., 2007). Corresponding to these complex current systems, the shelf break and slope regions of the Chukchi Sea in the Arctic Ocean show three layers: a warm surface layer, a cold intermediate layer, and a warm deep layer (Corlett & Pickart, 2017). The cold intermediate layer consists of both Pacific winter water and remnant winter water (RWW). Newly ventilated winter

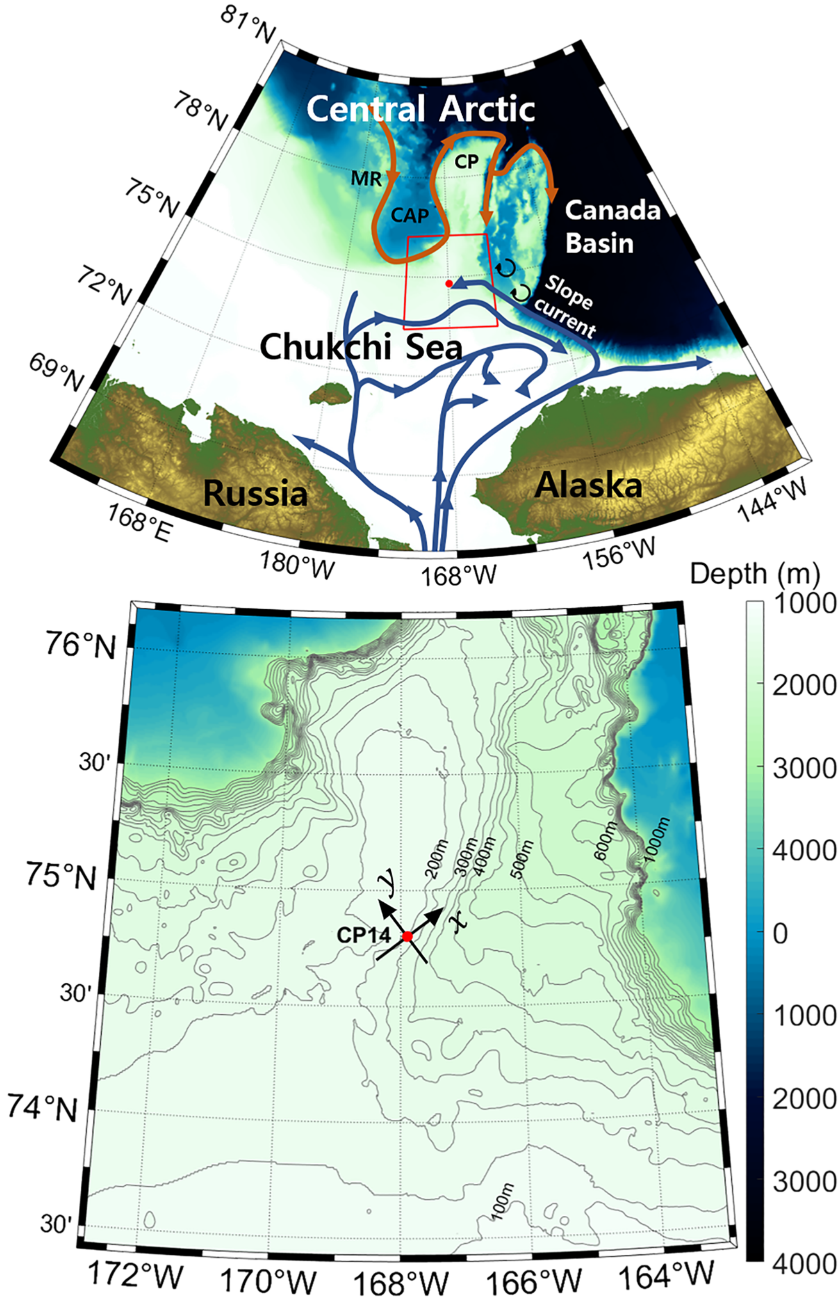

Figure 1. Bathymetry around the study area of the Chukchi Sea, Arctic Ocean. The lower panel is the enlargement of the red box in the upper figure, with the red dot representing the CP14 mooring site (74.80°N, 167.89°W). MR, CAP, and CP indicate the Mendeleev Ridge, Chukchi Abyssal Plain, and Chukchi Plateau, respectively. The blue lines indicate the intrusion of Pacific water and the slope current (Corlett & Pickart, 2017). The orange lines indicate the flow of the boundary currents along the topography (Woodgate et al., 2007). Black circles indicate sporadic eddies around the Chukchi slope. Gray contours indicate 50-m interval isobaths. *x* and *y* denote along- and cross-slope directions, respectively.

water is initially cold Pacific winter water; however, it is modified by mixing or solar heating to become RWW (Corlett & Pickart, 2017). The RWW and warm deep layer with a high salinity (~1 °C warmer and ~0.5 psu saltier than the RWW in observational data) create a relatively strong stratification at depths of 150–200 m on the shelf break of the Chukchi Sea, where topographic Rossby waves (TRWs) were observed from a mooring site in this study (Figure 1).

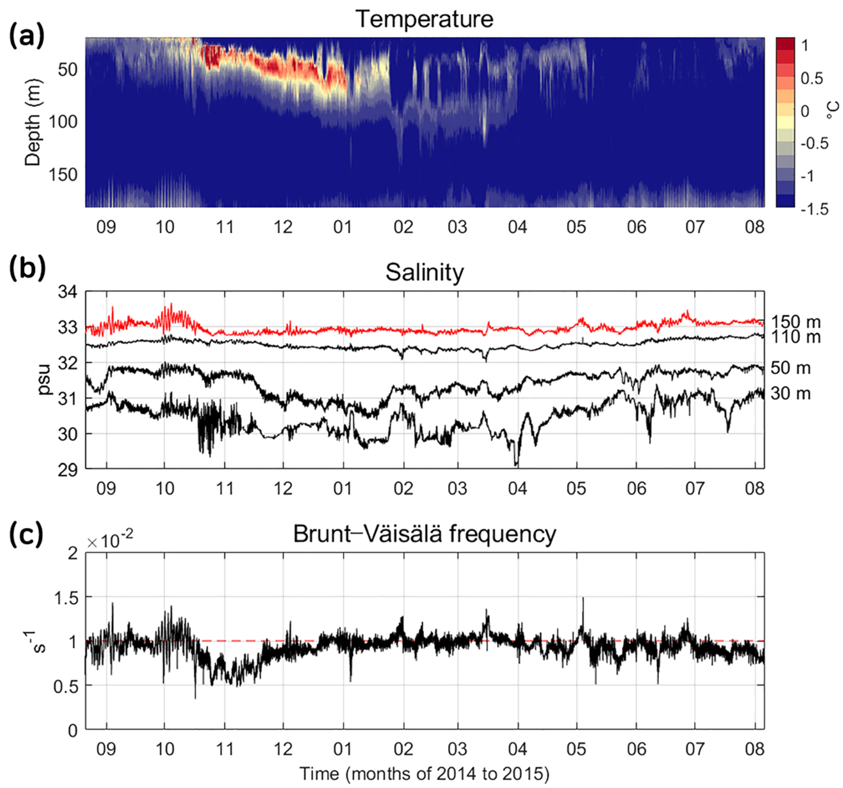

Figure 2. Time series of (a) temperature measured at 29 depths (2-m intervals from 20–30 m, 4-m intervals from 30–60 m, and 8-m intervals from 60–180 m), (b) salinity at four depths (30, 50, 110, and 150 m), with the red line indicating the salinity at 150 m, and (c) Brunt-Väisälä frequency $\left(N = \sqrt{-\frac{g}{\rho_0}\frac{\mathrm{d}\rho(z)}{\mathrm{d}z}}\right)$ calculated using the temperature and salinity data at 110- and 150-m depths, with the red dashed line representing 0.01 s^{-1}.

TRWs arise from the conservation of potential vorticity, which induces squeezing and stretching of the water column in regions of sloping topography (e.g., Hamilton, 2009; Meinen et al., 1993; Pickart, 1995; Rhines, 1970; Zhao & Timmermans, 2018). In the presence of stratification, the vertical structure of a TRW depends on its wavelength because strong stratification confines the motion near the bottom, acting like a rigid lid over a homogeneous fluid in compressing vortex lines (Rhines, 1970). Waves with a wavelength longer than the internal Rossby radius can have a barotropic structure, and the dispersion relation should be independent of stratification. Those shorter waves were termed bottom-trapped TRWs or edge waves by Rhines (1970) because stratification strongly constrains wave motions, causing an intensified oscillation near the bottom (see Appendix A).

Previous studies have analyzed TRWs in the Arctic Ocean, with some of these studies utilizing observations in the Beaufort Sea, adjacent to the study area (e.g., Timmermans et al., 2010; Zhao & Timmermans, 2018). Using velocity and sea level data, Zakharchuk (2009) observed internal Kelvin waves and barotropic and baroclinic topographic waves at 35- to 70-m depth. These were forced by winds on the continental shelf of the southern Chukchi Sea close to the Bering Strait. Zhao and Timmermans (2018) observed TRWs with periods of approximately 30–50 and 100–300 days from a 5-year time series of horizontal velocity and temperature data. They analyzed characteristics consistent with TRW theory in the limit of weak decay because the TRWs were observed below the halocline where stratification is weak. In this study, we focus on bottom-trapped TRWs observed at ~200-m depth, where stratification is relatively strong due to the cold intermediate and warm deep layers with high salinity. We assume that the stratification effect is equally important as the sloping bottom effect on TRWs.

Internal and inertial waves are known to enhance diapycnal mixing in the Arctic Ocean and can affect the circulation of the Arctic by altering the turbulent kinetic energy and vertical distribution of ocean heat

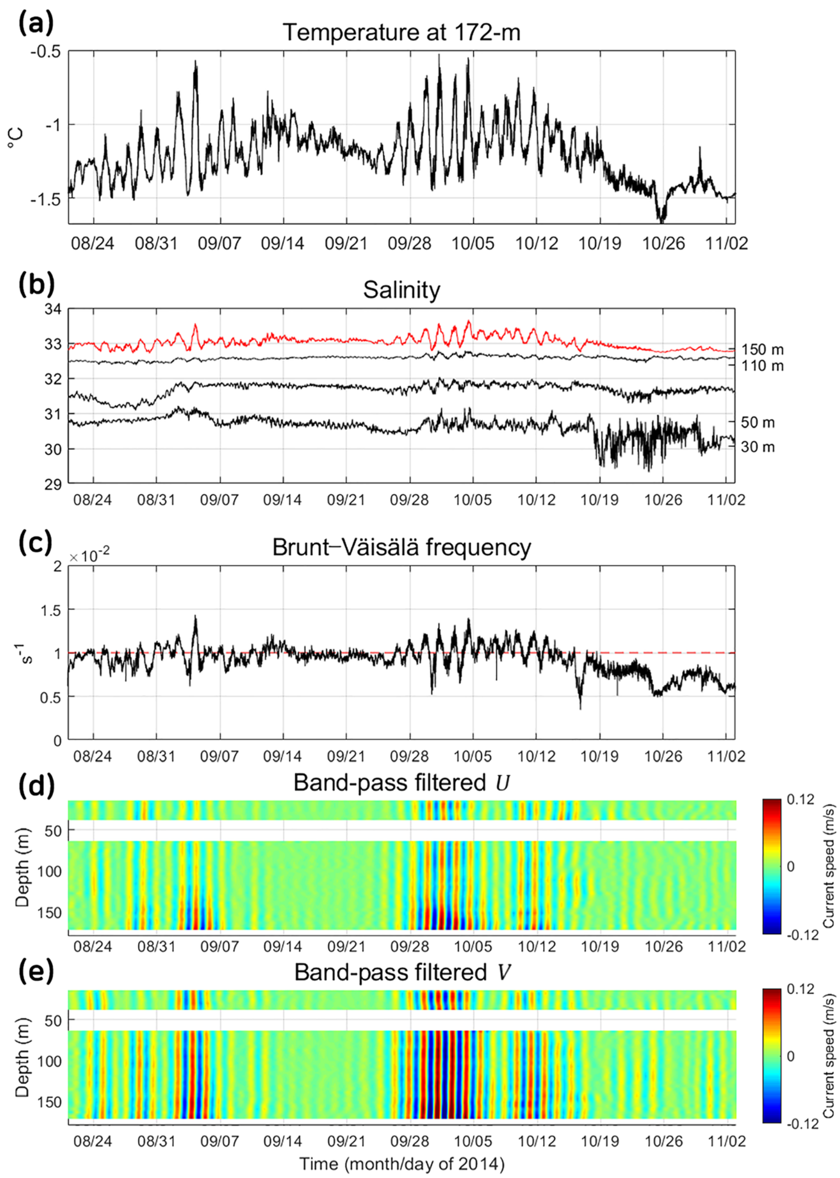

Figure 3. (a) Time series of the temperature at 172-m depth from late August to early November and expanded time series of the (b) salinity and (c) Brunt-Väisälä frequency (N) of Figure 2. Time series of (d) 30- to 50-hr band-pass filtered along-slope velocity (U) and (e) cross-slope velocity (V) during the same period of (a)–(c).

(e.g., Kawaguchi et al., 2015, 2016; Rainville & Woodgate, 2009). In addition to those waves, TRWs are expected to drive cross-slope advection, which can move waters on and off the shelf, affecting the seawater exchange between the shallow continental shelf and the deep ocean and having the potential to enhance diapycnal ocean mixing. TRWs in the shelf region are associated with energy propagation (Maslowski, 1996), onshore momentum flux and mixing (especially when their period is less than a few days; Garrett, 1978), and isopycnal diffusion (Nilsen et al., 2006). Moreover, Galt (1973) shows that they can play a dominant role in the development and maintenance of the general circulation of the Arctic Ocean because they are able to intensify the current along the boundaries. Nevertheless, they have not been extensively studied.

Here, we investigate the behavior of TRWs using temperature and horizontal velocity data collected from the shelf break of the Chukchi Sea. We identify TRW features from the observed data (section 2) and confirm their characteristics from theoretical estimates using in situ measured temperature and topography data

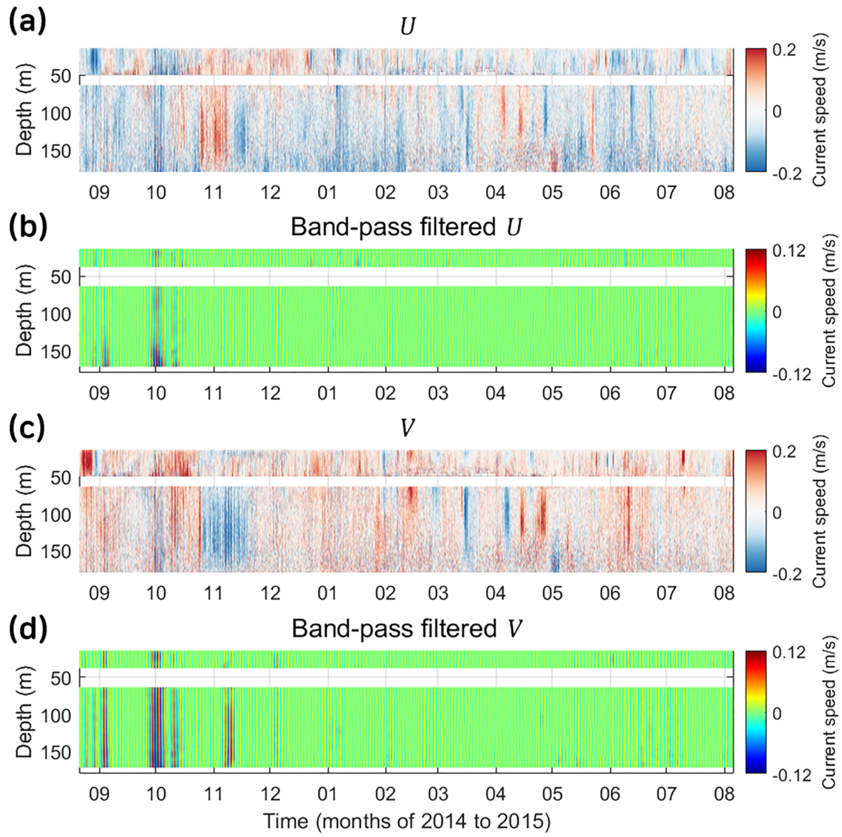

Figure 4. Time series of (a) along-slope velocity (U), (b) 30- to 50-hr band-pass filtered U, (c) cross-slope velocity (V), and (d) 30- to 50-hr band-pass filtered V.

(section 3). Moreover, we determine the variation of TRWs linked to seasonal changes of sea ice and local wind stress. We then explore the relationship between TRWs and local wind stress (section 4). We present our conclusions in section 5.

2. Data and Methods

The observational data analyzed in this study were collected from a mooring (CP14) deployed at 194-m depth on the shelf break of the Chukchi Sea (74.80°N and 167.89°W; Figure 1), where TRWs are observed. The mooring was equipped with an upward looking acoustic Doppler current profiler (ADCP; Workhorse sentinel 600 kHz) at approximately 58 m, a downward looking ADCP (Workhorse sentinel 300 kHz) at approximately 63 m, 29 temperature sensors (Sea Bird Electronics [SBE] 56 and SBE 37-SM), and four salinity sensors (SBE 37-SM). The bin size of the ADCPs was set to 4 m. Temperature sensors were installed at 2-m intervals from 20 to 30 m, 4-m intervals from 30 to 60 m, and 8-m intervals from 60 to 180 m. Salinity sensors were installed at 33, 53, 110, and 150 m. Data were collected for approximately 1 year from 21 August 2014 to 5 August 2015 at intervals of 45 min for ADCPs and 1 min for temperature and salinity sensors.

Current data at a depth of 172 m were used as the nearest data to the bottom because deeper data were contaminated by bottom reflections. For prior understanding of observed TRWs, ADCP-measured velocity data were decomposed into the along-slope (x) and cross-slope (y) components (Figure 1). U is the velocity component in x, and V is the velocity component in y. A third-order Butterworth band-pass filter was utilized to confirm the signals of the TRWs from the time series of U and V. We determined the band-pass cutoffs at 30 and 50 hr because the 30-hr cutoff can get rid of diurnal tidal energy and the observed TRW signals show high energy at this band not only in current measurements but also in temperature measurements as will be shown later. The Brunt-Väisälä frequency (N) was calculated using temperature and salinity data.

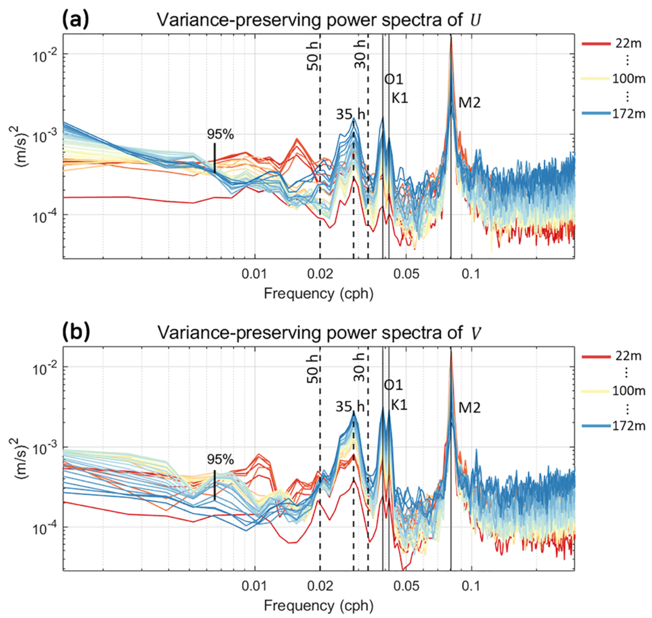

Figure 5. Variance-preserving power spectra of (a) along-slope velocity (U) and (b) cross-slope velocity (V). Colors change depending on depth, that is, 22 m (red) is the shallowest and 172 m (dark blue) is the deepest depth. Vertical, black dashed lines denote 30- and 50-hr periods. The 95% confidence levels are indicated by thick black lines. Thin black lines indicate the tidal component of O1 (0.039 cph), K1 (0.042 cph), and M2 (0.081 cph). The inertial frequency at the location of mooring CP14 is 0.080 cph, very close to the frequency for M2.

Salinity, measured at only four depths, was assumed to be vertically linear in estimating the buoyancy frequency at 110- and 150-m depths.

Bathymetry data with a 30 arc sec resolution from International Bathymetric Chart of the Arctic Ocean, Version 3.0 (Jakobsson et al., 2012) were used to calculate the bottom slope and to set the local x and y coordinate system around the mooring site. The bottom slope was calculated from the depth gradient in the cross-slope direction. Sea ice concentration data (MASAM2: Daily 4-km Arctic Sea Ice Concentration, Version 1) were obtained from the National Snow and Ice Data Center (Fetterer et al., 2015). Data within 40 km of the mooring site were averaged to produce a spatially smoothed time series of sea ice concentration. The surface wind stress data at the nearest point to mooring CP14 were obtained from the ERA-Interim daily European Centre for Medium-Range Weather Forecasts reanalysis data set, with 0.125° resolution. These data were used to determine the relationship among the sea ice concentration, wind stress, and TRWs.

We used the cross-spectral analysis between V and the near-bottom temperature to show evidence for TRWs, as performed by Thompson and Luyten (1976). For a profile with a temperature with increasing with depth, such as the one considered here, the temperature increases (decreases) due to the upslope (downslope) motion of water, which is coupled with horizontal motions in the cross-slope direction, V.

Fourier transforms are commonly used to diagnose the amount of energy contained around a specific period (frequency). However, it cannot resolve how the energy changes in time, as is the case considered here, where the energy of TRWs shows annual variation. Therefore, we use the continuous wavelet transform (CWT) in addition to the Fourier transform. Broadly speaking, CWT is similar to the Fourier transforms but can resolve the time variation of spectral energy and seems to be most suitable to our case, showing annual variation (e.g., Grinsted et al., 2004). To analyze the CWTs of two time series together, a cross-wavelet transform (XWT) is commonly used. This technique finds regions in the time-frequency space where the time series shows a high common power and common significant values in two CWTs, which can imply the relationship between the two time series (Camayo & Campos, 2006; Grinsted et al., 2004). XWTs were used to show the relationship between the observed current at 172-m depth and the temporal change in the local wind turbulent surface stress. The statistical significance of CWTs and XWTs with a 95% significance level was evaluated with the null hypothesis that the signal is generated by a stationary process with a given background spectrum (cf. Grinsted et al., 2004).

3. Observations and Theoretical Aspects of TRWs

The time series of the temperature and salinity profiles (Figures 2a and 2b, respectively) show the cold intermediate water at approximate depths of 50–150 m and warm deepwater layers at approximate depths of 150–180 m. The 1-year-averaged temperatures observed at 100 and 182 m (the deepest sensor, 12 m above seabed) were −1.12 °C and −0.1 °C, representing the cold intermediate water and warm deep water, respectively. Except for about 1 month from mid-October to mid-November 2014, warm deep water was always present near the bottom of the profile. The salinity was approximately 32.6 and 33 psu at 110 and 150 m, respectively, throughout the observation period. Thus, the warmer and denser water observed below ~150 m was consistent with the general water mass distribution along the shelf break of the Chukchi Sea (Corlett & Pickart, 2017), with cold intermediate water overlaying warmer deep water. Figure 2c shows the time series of the Brunt-Väisälä frequency (N), calculated using the observed temperature and salinity data. N was stable at ~0.01 s^{-1} throughout the year, except for a month-long period from mid-October.

The time series of the temperature profiles showed fluctuations with a period of approximately 35 hr, especially below 150-m depth, where warm deep water existed (Figure 3a). These fluctuations were also evident in the 30- to 50-hr band-pass filtered along-slope velocity (U) and cross-slope velocity (V; Figures 3d and 3e).

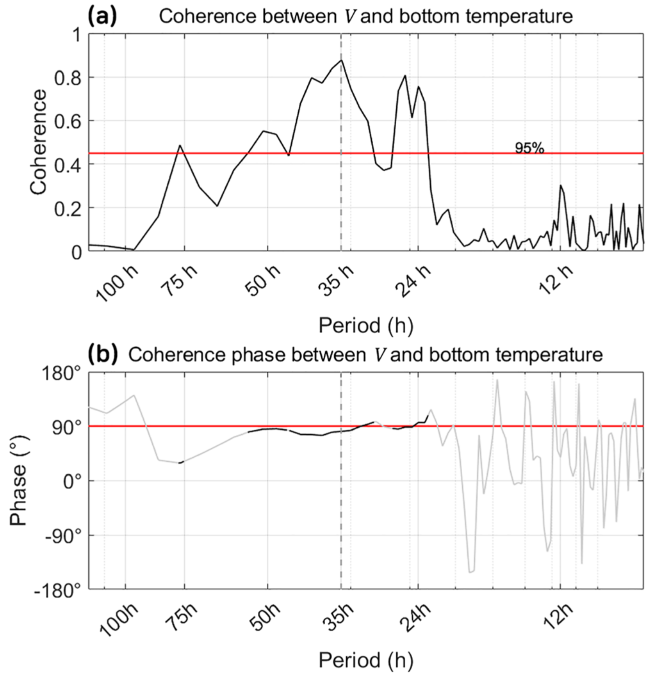

Figure 6. (a) Coherence and (b) coherence phase between the cross-slope velocity (V) at 172-m depth and the near-bottom temperature at the same depth as V. Red lines in (a) and (b) indicate the 95% confidence level and 90°, respectively. Dashed gray lines indicate the 35-hr period. A positiv phase means that velocity leads temperature, whereas a negative phase means that temperature leads velocity. Phase is gray colored if coherence is lower than the 95% significance level.

The near-bottom currents of the band-pass filtered U and V were stronger than those in the upper layers. They exhibited energetic subinertial fluctuations in early September and early October 2014 (Figures 4b and 4d). The fluctuations weakened from November 2014 until June 2015.

Fourier transforms were applied to investigate the current fluctuations as a function of frequency. Figure 5 reveals prominent peaks caused by semidiurnal tides and inertial motions (~0.08 cph) and diurnal tides (~0.04 cph), which are the subject of ongoing research. Notably, there was also a significant peak at 0.029 cph (about 35-hr period), which was as strong as the diurnal peak. The current fluctuations with ~35-hr periods were more energetic nearer to the bottom than the surface; bottom-intensified fluctuations are a typical feature of TRWs (e.g., Rhines, 1970; Thompson & Luyten, 1976). The fluctuations with ~35-hr periods were more energetic for V than for U.

Figure 6 shows the coherence squared (hereafter, coherence) and coherence phase between V and the near-bottom temperature. The coherence at ~35-hr periods was 0.86, and the coherence phase at the same period was almost 90°. The coherence phase (Figure 6b) showed a velocity-leading coherence phase, that is, the highest temperature occurred when water particles were moved to the highest level by the upslope motion.

The vertical profile of current speed $\left(\sqrt{U^2+V^2}\right)$ based on 30- to 50-hr band-passed currents for the period when energetic TRW events occurred in September and October 2014 shows the bottom-trapped structure (Figure 7). For bottom-trapped waves in a stratified ocean over sloping topography, a current having a wave-like form can be represented by a hyperbolic cosine ($\cosh(\mu z)$, where μ is the bottom-trapping coefficient and z is the depth A4). Therefore, the vertical structure of the observed current speed was fitted to $S = S_0 \times \cosh(\mu z)$, where S_0 is the current speed at the nearest depth to the surface (63 m in the fitted data as only the downward looking ADCP data were used). The bottom-trapping coefficient determined from the fitted profile (μ_o) was 0.03 m^{-1}, and the observed bottom-trapping depth (h_o) was 33 m. For wavelengths $\lambda = \frac{2\pi}{K_h}$ that are sufficiently shorter than the internal Rossby radius $\left(\frac{NH_0}{f_0}\right)$, the vertical structure is bottom trapped. In other words, the vertical structure is bottom trapped in the case of $\frac{NH_0K_h}{f_0} \gg 1$. With our estimate of μ_o (which was nearly the same as $\frac{NK_h}{f_0}$ based on the dispersion relation; A5), $\mu H_0\left(\frac{NH_0K_h}{f_0}\right)$ was about 6, sufficiently larger than 1. Therefore, the wavelength of the observed current fluctuations was indeed much shorter than the internal Rossby radius. Since the topographic beta effect is expected to be dominant over the planetary beta effect, the vertical profiles of the pressure and dispersion relation, respectively, are as follows:

$$p \sim \frac{1}{2} e^{[i(kx+ly-\omega t)-\mu z]}, \tag{1}$$

$$\omega = -\alpha N \frac{k}{K_h} = \alpha N \sin\theta, \tag{2}$$

where θ is the angle of the wavenumber vector measured from the y axis (Figure 8), (k, l) are the x and y components of the wavenumber vector (Figure 8), and ω is the frequency. A more complete derivation of Equations 1 and 2 is given in Appendix A.

A better understanding of the observed TRWs can be gained by substituting the environmental parameters of the study area to the vertical profile 1 and dispersion relation 2. Table 1 lists the environmental parameters used and the derived TRW characteristics. We considered N to be a constant because it is fairly stable except

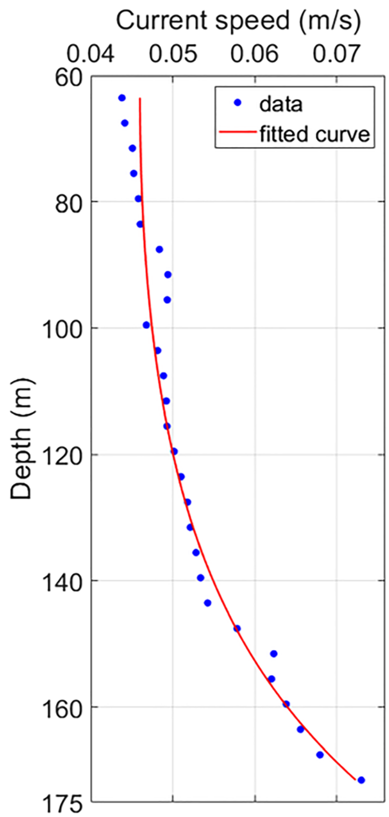

Figure 7. Vertical structure of the mean current speed during September–October 2014 when the two energetic TRW events occurred (~40 days). The blue dots and red curve denote, respectively, observations and their least squares fitting with a $S_0 \times \cosh(\mu z)$ function, where S_0 is the current speed at 63 m, μ is the bottom-trapping coefficient, and z is the depth.

for the 1-month period from mid-October (Figure 2c). The average value of N for the observation period was 0.0093 s^{-1}. Two available CTD profiles on 21 August 2014 and 5 August 2015 around the mooring site (not shown here) indicated that N near the bottom was also about 0.01 s^{-1}. The approximate frequencies of TRWs can be inferred from N and α. From Equation 2, the frequencies of bottom-trapped TRW were less than or equal to αN, that is, $T \geq 2\pi/\alpha N$, where T is the TRW period. In the study area, T was estimated to be ~27 hr. It was reasonably close to the observed 35-hr period of bottom-trapped TRWs in consideration of the uncertainty of the values used for N and α.

The frequency of TRWs is independent of the wavelength but depends on the direction of the wave vector (Equation 2). With an observed frequency of 0.029 cph, the angle of the wavenumber vector θ was estimated to be approximately 50° from the downslope direction. For plane waves, the direction of wave propagation is perpendicular to the direction of particle excursion, which is equivalent to the observed principal axis of currents, as reported by Thompson and Luyten (1976). In our case, the angle of the principal axis of currents φ was 155° from the downslope, so θ and φ were close to perpendicular (Table 1). Therefore, the theoretical direction of wave propagation was similar to the observation, and the water parcel motion was predominantly in the cross-slope direction (Figure 8).

The wavenumber vector K_h can be deduced from the dispersion relation and environmental parameters. Because the wave energy varies with the square of $\cosh(\mu z)$, K_h can be calculated using the ratio (R) of the energy between two depths, $R = \left(\frac{\cosh\left(\frac{K_h N}{f_0} z_1\right)}{\cosh\left(\frac{K_h N}{f_0} z_2\right)}\right)^2$ (cf. A10 and Thompson & Luyten, 1976). The energy ratio R is calculated from the power spectra of kinetic energy (not shown here but similar to the results shown in Figure 5). The estimated K_h, λ, and phase velocity (C) were 0.4 km^{-1}, 17 km, and 0.48 km hr^{-1}, respectively (Figure 8). The calculated wavelength was 17 km, and R_d was approximately 14 km, which was comparable to the known value 15 km (Nurser & Bacon, 2014). These values give $\mu H_0 = \frac{N H_0 K_h}{f_0}$~6, which indeed satisfies the condition of bottom trapping $\mu H_0 \gg 1$. Using the estimated K_h, μ, and h, we can estimate $\mu_b = \frac{f_0 L}{N} = 0.026$ m^{-1} and $h_b = 38$ m, where subscript b denotes the calculated value using the estimated K_h. They were similar to μ_o and h_o deduced earlier from the vertical profile (Table 1). It follows that the product of estimated K_h and R_d was also greater than the unity $\left(\frac{N H_0 K_h}{f_0} = 5.2\right)$, indicating once again that the wave was bottom trapped.

4. Causes and Consequences of TRWs

Energetic TRW occurrences (Figure 9a) coincided with decreased sea ice concentrations, as seen in the time series in Figure 9b. We can infer that TRWs are inhibited from receiving wind forcing by the sea ice because it forms a physical barrier that can significantly reduce momentum fluxes from the wind to the ocean (Lubin & Massom, 2006). Two energetic TRW events occurred during the sea ice-free season, as shown in Figure 9a. The wavelet power of V in the 30- to 50-hr bands showed two remarkable peaks in early September and early October and then weakened by November. As shown in Figure 9b, the sea ice in the study area had completely melted by September 2014; it started to freeze again in mid-October, and the ice cover was almost 100% until June 2015. Once the sea ice cover was near 100%, the TRW events were relatively weak. Strong wind events (wind speed >12 m s^{-1}) coincided with the occurrence of TRWs in early September and early October (Figure 9c), when there was a sudden temporal change in wind stress (Figure 9c). TRWs did not

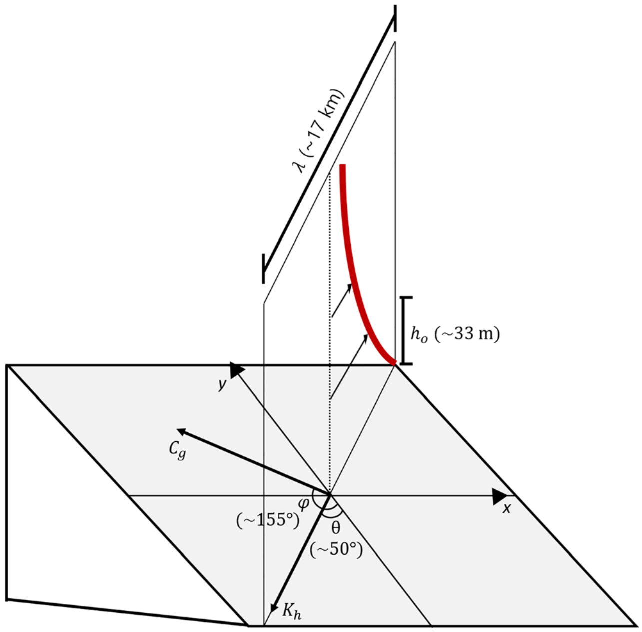

Figure 8. A schematic describing the characteristics of the observed TRWs. λ and h_o indicate the wavelength and bottom-trapping depth estimated by fitting the hyperbolic cosine to the horizontal velocity data, respectively. K_h indicates the direction of the horizontal wavenumber vector, which is perpendicular to the direction of the group velocity (C_g). θ and φ indicate the angle of the wavenumber vector clockwise from the downslope direction and the angle of the principal axis of velocity with a period of 35 hr, respectively. The red line represents the bottom-intensified current structure due to TRWs.

well develop in mid-September and mid-October when wind stress was consistently strong (between pink patches in Figure 9d). After November, the signal of the TRW events was weaker than in September–October, although the winds were even stronger.

CWTs of V, the local wind turbulent surface stress τ, and the temporal change of local wind turbulent surface stress (d|τ|/dt) were performed to better understand the significant variations in TRWs and wind events in the time and frequency domains (Figure 10). The CWT of V (Figure 10a) shows the variations in the TRW events in 30- to 50-hr bands. Two significant and energetic TRW events were identified, along with other significant events during the sea ice-covered season. Figures 10b and 10c show the CWT of τ and d|τ|/dt, respectively, with significant areas of ~1- to 8-day bands when wind events occurred. The CWT of V and d|τ|/dt shows that the strong TRW events and the temporal change of wind stress overlapped in time.

The XWT analysis (Grinsted et al., 2004) confirmed the relationship between TRW events and local wind stress. As shown in Figure 11a, a strong similarity was also observed in the 30- to 50-hr bands at the time of TRW events, which was also observed during the sea ice-covered season. Figure 11b shows the normalized strength of V and d|τ|/dt in the 30- to 50-hr bands, which influenced the XWT in the 30- to 50-hr bands. TRW and wind events occurred at similar times. These results strongly signify that TRWs are triggered by the change in local wind stress and that sea ice weakens the momentum flux of the wind stress to the ocean during the sea ice-covered season.

One of the factors that can trigger TRWs is wind stress (e.g., Adams & Buchwald, 1969; Csanady, 1975; Schlichtholz, 2002; Shilo et al., 2007; Simons, 1975). TRWs are induced by cross-isobaric motions as the fluid column is stretched and compressed over the sloping bottom to conserve potential vorticity (Kim et al., 2013; Oey & Lee, 2002). Therefore, we speculate that horizontal water mass transport excited by the wind stress caused an extension of the vertical motion to greater depths (~200 m), which can provide a restoring tendency for TRWs over a slope. These results, which show that strong TRWs during the sea ice-free season are related to the local wind forcing, imply that energetic TRW events on the shelf break of the Chukchi Sea could be generated more frequently with increasing sea ice loss in the Chukchi Sea.

The TRWs showed a dominant velocity component in the cross-slope direction. This implies that the water parcel motion was predominantly in the across-slope direction, and the restoring effect of the slope was

Table 1
Environmental Parameters of the Study Area and the Observed and Calculated Characteristics of TRWs

Symbol	Value	Explanation
f_0 (s^{-1})	1.404×10^{-4}	Representative Coriolis parameter
N (s^{-1})	0.0093	Brunt-Väisälä frequency
H_0 (m)	194	Bottom depth
α	0.007	Bottom slope
R_d (km)	14	Internal Rossby radius
θ (°)	50	Angle of the wavenumber vector clockwise from the downslope direction
φ (°)	155	Angle of the principal axis of velocity with a period of 35 hr
h_b (m)	38	Calculated bottom-trapping depth
h_o (m)	33	Observed bottom-trapping depth estimated by fitting the hyperbolic cosine to the horizontal velocity data
K_h (km^{-1})	0.4	Amplitude of the horizontal wavenumber vector
λ (km)	17	Wavelength
C (km hr^{-1})	0.48	Phase velocity

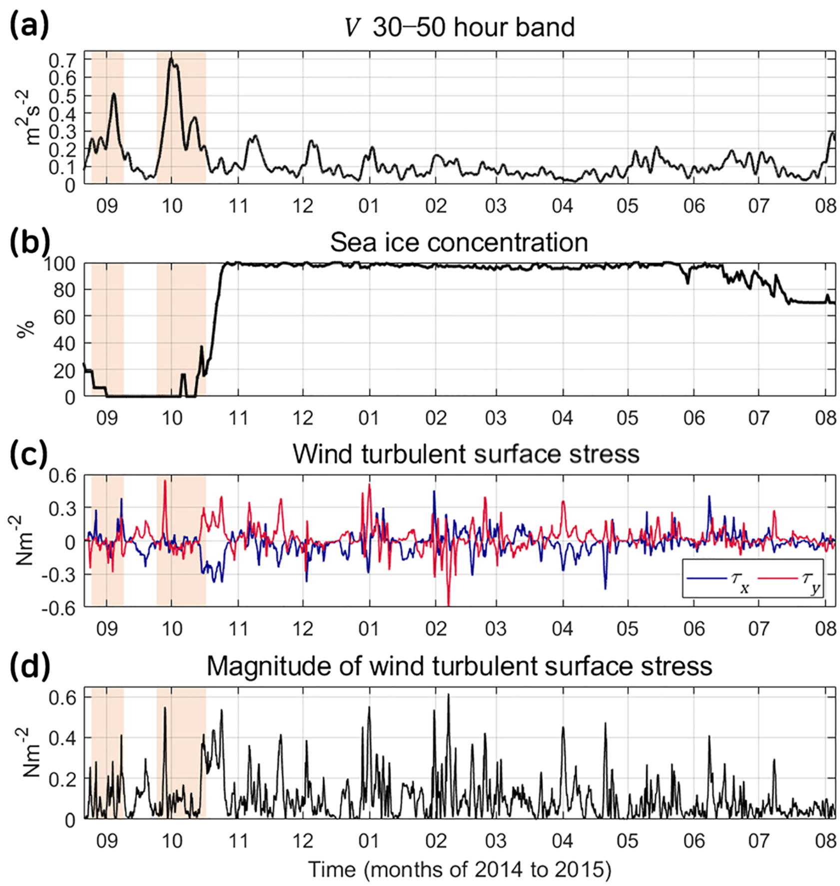

Figure 9. Time series of (a) the wavelet power of cross-slope velocity (V) in 30- to 50-hr bands, (b) sea ice concentration around the study area obtained from the National Snow and Ice Data Center, (c) wind turbulent surface stress around the study area obtained from ECMWF reanalysis data, and (d) the magnitude of wind turbulent surface stress. Apricot patches indicate the two energetic TRW events during the sea ice-free season.

larger than the case when the along-slope velocity was dominant because it had a relatively high frequency (Thompson & Luyten, 1976; Zhao & Timmermans, 2018). Therefore, TRWs in the cross-slope dominant direction and at relatively high frequency can affect the seawater exchange between water layers on the shelf break of the Chukchi Sea, with the potential to enhance diapycnal ocean mixing because of enhanced vertical shear caused by bottom-intensified TRWs as shown by Fer et al. (2010). These are known to be important to halocline water formation (Rainville et al., 2011) and can modify water properties. A change in water properties could have profound effects on the circulation in the Arctic Ocean and sea ice (e.g., Carmack et al., 2015; Comiso et al., 2008; Perovich, 2011). In addition, TRW-induced mixing processes may influence the distribution of the chlorophyll α maximum at 30- to 60-m layers over the shelf break of the Chukchi Sea, by supplying nutrients from the temperature-minimum intermediate layer, where nutrients are abundant (Nishino et al., 2008; Torres-Valdés et al., 2013).

5. Conclusions

Horizontal current velocity, water temperature, and salinity data collected from a mooring located on the shelf break of the Chukchi Sea (74.80°N, 167.89°W) were analyzed to determine the major features of TRWs. Time series of along-slope and cross-slope directional velocity data revealed bottom-trapped TRWs with a period of 35 hr. There was a significant coherence between the near-bottom temperature and upslope velocity, with a value of 0.86 at 35-hr periods. The coherence phase at 35 hr was almost 90°. These results provide evidence for TRWs because vertical motions represented by temperature fluctuations should result from horizontal fluctuations on steep topography.

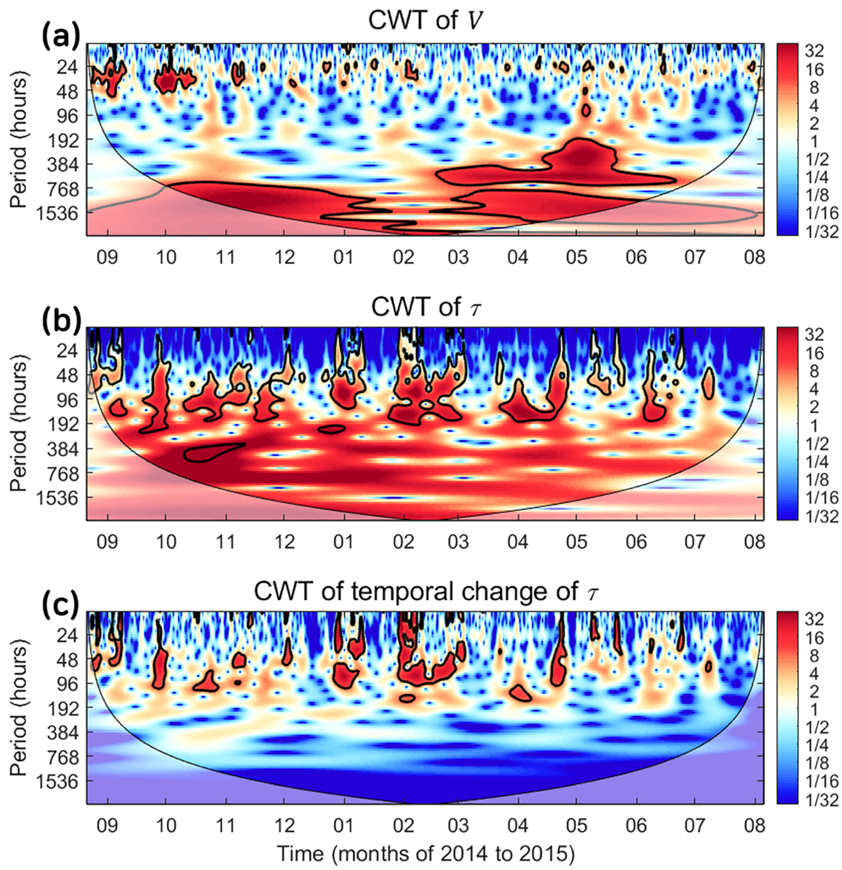

Figure 10. Continuous wavelet transform (CWT) of (a) the cross-slope velocity (V) at 172-m depth, (b) the magnitude wind turbulent surface stress τ obtained from ECMWF reanalysis data, and (c) the temporal change in τ (d|τ|/dt). Black contours indicate the 95% significant level, and the opaque area indicates the 95% confidence level.

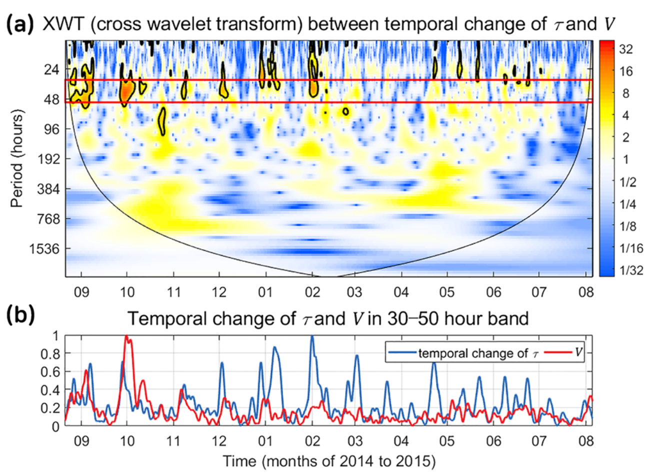

Figure 11. (a) Cross-wavelet transform between the cross-slope velocity (V) and the temporal change in the wind turbulent surface stress (d|τ|/dt) obtained from ECMWF reanalysis data and (b) time series of the normalized wavelet power of V and d|τ|/dt in 30- to 50-hr bands. Black contours indicate the 95% significant level, and the opaque areas indicate values lower than the 95% confidence level.

The theoretical characteristics of TRWs were calculated by substituting the environmental parameters fitted to the study area to the linear dispersion relationship (Pedlosky, 1987). The wavelength, angle of the wavenumber vector, and bottom-trapping depth were calculated. The observed characteristics of TRWs were confirmed to be similar to those calculated theoretically. Their shortwave period, short wavelength, cross-slope direction of the wavenumber vector, and shallow bottom-trapping depth indicate that the TRW characteristics were affected by stratification.

Energetic TRW events occurred during the sea ice-free season, whereas TRW signals typically became weak during the season with sea ice cover. Since sea ice forms a physical barrier that prohibits momentum fluxes from the wind to the ocean (Lubin & Massom, 2006), we conclude that sea ice inhibits the generation of wind-induced TRWs. XWT analyses performed between the change in local wind stress and velocity revealed a significant common power at the 35-hr bands, which could be represented by wind-induced TRWs. This signifies that a longer ice-free season may allow for more frequent occurrences of energetic TRWs, which may affect seawater exchange and mixing on the shelf break of the Chukchi Sea. More studies should be conducted on TRWs to better understand the physical processes modifying the water properties in the Chukchi Sea of the Arctic Ocean, where the melt rate of sea ice is continuously increasing (Mioduszewski et al., 2019).

Data Availability Statement

The processed data used in figures and tables can be found **online (**https://doi.org/10.17882/74244**)**.

Appendix A: TRWs in a Stratified Ocean

Consider the propagation of Rossby waves in a stratified ocean with a rigid top and a uniformly sloping bottom. For a small enough bottom slope α, such that the fractional depth change is negligible, $\frac{\alpha L}{H_0} \ll 1$, where L is the length scale and H_0 is the typical depth of the ocean, the first-order quasi-geostrophic equation for potential vorticity conservation, in terms of perturbation pressure p, is given by

$$\frac{\partial}{\partial t}\left[\nabla^2 p + \frac{{f_0}^2 \partial^2 p}{N^2 \partial z^2}\right] + \beta \frac{\partial p}{\partial x} = 0, \quad \text{(A1)}$$

where t is time, f_0 is the representative Coriolis parameter, and (x, y) are the axes in the along-slope and upslope directions. No normal flow boundary conditions at the sea surface and seafloor are

$$\frac{\partial p}{\partial z} = 0 \text{ at } z = 0, \quad \text{(A2)}$$

$$\frac{\partial^2 p}{\partial t \partial z} = \frac{\alpha N^2}{f_0} \frac{\partial p}{\partial x} \text{ at } z = -H_0. \quad \text{(A3)}$$

For waves dominated by topography, that is, for $\beta = 0$, solutions are obtained (Leblond & Mysak, 1978; Pedlosky, 1987; Rhines, 1970) for p having the wave-like form

$$p \sim e^{i(kx+ly-\omega t)} \cosh(\mu z), \quad \text{(A4)}$$

where (k, l) are the (x, y) components of the wavenumber and $\mu = \frac{NK_h}{f_0} = N\left(k^2+l^2\right)^{1/2}/f_0$. Substituting A4 into A3 gives the dispersion relation

$$\omega = -\alpha N \left(\frac{k}{K_h}\right) \coth(\mu H_0). \quad \text{(A5)}$$

Since $\omega > 0$, A5 implies that $k < 0$, that is, waves propagate with upslope direction (positive y direction) on their right. For waves with longer wavelengths compared to the internal Rossby radius NH_0/f_0, that is, $\mu H_0 = \frac{NH_0 K_h}{f_0} \ll 1$, A4 and A5 can be approximated to

$$p \sim e^{i(kx+ly-\omega t)}, \quad \text{(A6)}$$

and

$$\omega = -\frac{\alpha f_0}{H_0} \frac{k}{K_h^2}. \quad \text{(A7)}$$

Thus, the pressure perturbation, hence the current, is uniform with depth, implying barotropic motion, and the dispersion relation is independent of stratification.

For short waves, which we focus on, that is, for $\mu H_0 = \frac{NH_0 K_h}{f_0} \gg 1$, A4 and A5 can be approximated to

$$p \sim \frac{1}{2} e^{[i(kx+ly-\omega t)-\mu z]}, \quad \text{(A8)}$$

and

$$\omega = -\alpha N \frac{k}{K_h} = \alpha N \sin\theta, \tag{A9}$$

where θ is the angle of the wavenumber vector measured from the y axis. The pressure perturbation and the current are trapped at the bottom with the vertical scale $\mu^{-1} = \frac{f_0}{NK_h} \sim f_0 L/N$. From A9, the frequency of the bottom-trapped wave is upper bounded with the maximum value $\omega_{\max} = \alpha N$. This happens when waves propagate in the along-slope direction. The wave-averaged kinetic energy at depth z, $E(z)$, is given by

$$E(z) \sim <\nabla p \cdot \nabla p> \sim \cosh^2(\mu z), \tag{A10}$$

where $< >$ means wave averaging.

Acknowledgments
This study was supported by the "Test of underwater observation data transfer system using a pop-up buoy in extremely severe environment" project, supported by the "Korea-Arctic Ocean Observing System (K-AOOS; KOPRI (Korea Polar Research Institute), 20160245)," funded by the MOF, Korea. Support for this research was also provided by the Office of Naval Research Global grant (N62909-17-1-2041). We would like to thank to two reviewers and editor for their useful comments and suggestions that improved this manuscript.

References

Adams, J. K., & Buchwald, V. T. (1969). The generation of continental shelf waves. *Journal of Fluid Mechanics*, *35*(4), 815–826. https://doi.org/10.1017/S0022112069001455

Camayo, R., & Campos, E. J. D. (2006). Application of wavelet transform in the study of coastal trapped waves off the west coast of South America. *Geophysical Research Letters*, *33*, L22601. https://doi.org/10.1029/2006GL026395

Carmack, E. I., Polyakov, L., Padman, I., Fer, E., Hunke, J., Hutchings, J., et al. (2015). Toward quantifying the increasing role of oceanic heat in sea ice loss in the new Arctic. *Bulletin of the American Meteorological Society*, *96*(12), 2079–2105. https://doi.org/10.1175/BAMS-D-13-00177.1

Comiso, J. C., Parkinson, C. L., Gersten, R., & Stock, L. (2008). Accelerated decline in the Arctic sea ice cover. *Geophysical Research Letters*, *35*, L01703. https://doi.org/10.1029/2007GL031972

Corlett, W. B., & Pickart, R. S. (2017). The Chukchi slope current. *Progress in Oceanography*, *153*, 50–65. https://doi.org/10.1016/j.pocean.2017.04.005

Csanady, G. T. (1975). Topographic waves in Lake Ontario. *Journal of Physical Oceanography*, *6*, 93–103. https://doi.org/10.1175/1520-0485(1976)006<0093:TWILO>2.0CO;2

Fer, I., Skogseth, R., & Geyer, F. (2010). Internal waves and mixing in the marginal ice zone near the Yermark Plateau. *Journal of Physical Oceanography*, *40*(7), 1613–1630. https://doi.org/10.1175/2010JPO4371.1

Fetterer, F., Stewart, J. S., & Meier, W. N. (2015). *Updated daily, MASAM2: Daily 4 km Arctic sea ice concentration, version 1*. Boulder, Colorado USA: NSIDC: National Snow and Ice Data Center. https://doi.org/10.7265/N5ZS2TFT

Galt, J. A. (1973). A numerical investigation of Arctic Ocean dynamics. *Journal of Physical Oceanography*, *3*(4), 379–396. https://doi.org/10.1175/1520-0485(1973)003<0379:ANIOAO>2.0.CO;2

Garrett, C. (1978). Topographic Rossby waves off east Australia: Identification and role in shelf circulation. *Journal of Physical Oceanography*, *9*, 244–253. https://doi.org/10.1175/1520-0485(1979)009<0244:trwoea>2.0.co;2

Grinsted, A., Moore, J. C., & Jevrejeva, S. (2004). Application of the cross wavelet transform and wavelet coherence to geophysical time series. *Nonlinear Processes in Geophysics*, *11*(5/6), 561–566. https://doi.org/10.5194/npg-11-561-2004

Hamilton, P. (2009). Topographic Rossby waves in Gulf of Mexico. *Progress in Oceanography*, *82*(1), 1–31. https://doi.org/10.1016/j.pocean.2009.04.019

Jakobsson, M., Mayer, L., Coakley, B., Dowdeswell, J. A., Forbes, S., Fridman, B., et al. (2012). The International Bathymetric Chart of the Arctic Ocean (IBCAO) version 3.0. *Geophysical Research Letters*, *39*, L12609. https://doi.org/10.1029/2012GL052219

Kawaguchi, Y., Nishino, S., & Inoue, J. (2015). Fixed-point observation of mixed layer evolution in the seasonally ice-free Chukchi Sea: Turbulent mixing due to gale winds and internal gravity waves. *Journal of Physical Oceanography*, *45*(3), 836–853. https://doi.org/10.1175/JPO-D-14-0149.1

Kawaguchi, Y., Nishino, S., Inoue, J., Maeno, K., Takeda, H., & Oshima, K. (2016). Enhanced diapycnal mixing due to near-inertial internal waves propagating through an anticyclonic eddy in the ice-free Chukchi Plateau. *Journal of Physical Oceanography*, *46*(8), 2457–2481. https://doi.org/10.1175/JPO-D-15-0150.1

Kim, Y.-B., Chang, K.-I., Park, J.-H., & Park, J. J. (2013). Variability of the Dokdo Abyssal Current observed in the Ulleung Interplain Gap of the East/Japan Sea. *Acta Oceanologica Sinica*, *32*(1), 12–23. https://doi.org/10.1007/s13131-013-0263-y

Leblond, P. H., & Mysak, L. A. (1978). *Waves in the Ocean*. Amsterdam Oxford New York: Elsevier Scientific Publishing Company. https://doi.org/10.1016/0377-0265(80)90007-x

Lubin, D., & Massom, R. (2006). Sea ice. In *Polar remote sensing*, *Atmosphere and Oceans* (Vol. 1, pp. 309–728). Chichester, UK: Springer.

Maslowski, W. (1996). Numerical simulations of topographic Rossby waves along the East Greenland Front. *Journal of Geophysical Research*, *101*(C4), 8775–8787. https://doi.org/10.1029/95JC03799

Meinen, C., Fields, E., Pickart, R. S., & Watts, D. R. (1993). Ray tracing on topographic Rossby waves. In *Technical Report, 93–1* (pp. 1–29). Kingston: University of Rhode Island.

Mioduszewski, J. R., Vavrus, S., Wang, M., Holland, M., & Landrum, L. (2019). Past and future interannual variability in Arctic sea ice in coupled climate models. *The Cryosphere*, *13*(1), 133–124. https://doi.org/10.5194/tc-13-113-2019

Nilsen, F., Gjevik, B., & Schauer, U. (2006). Cooling of the West Spitsbergen Current: Isopycnal diffusion by topographic vorticity waves. *Journal of Geophysical Research*, *111*, C08012. https://doi.org/10.1029/2005JC002991

Nishino, S., Shimada, K., Itoh, M., Yamamoto-Kawai, M., & Chiba, S. (2008). East-west differences in water mass, nutrient, and chlorophyll *a* distributions in the sea ice reduction region of the western Arctic Ocean. *Journal of Geophysical Research*, *111*, C08012. https://doi.org/10.1029/2005JC002991

Nurser, A. J. G., & Bacon, S. (2014). The Rossby radius in the Arctic Ocean. *Ocean Science*, *10*(6), 967–975. https://doi.org/10.5194/os-10-967-2014

Oey, L.-Y., & Lee, H.-C. (2002). Deep eddy energy and topographic Rossby waves in the Gulf of Mexico. *Journal of Physical Oceanography*, *32*(12), 3499–3527. https://doi.org/10.1175/1520-0485(2002)032<3499:DEEATR>2.0.CO;2

Pedlosky, J. (1987). *Geophysical fluid dynamics*, (2nd ed.). New York: Springler-Verlag. https://doi.org/10.1007/978-1-4612-4650-3

Perovich, D. K. (2011). The changing Arctic sea ice cover. *Oceanography*, *373*(2045), 162–173. https://doi.org/10.1098/rsta.2014.0165

Pickart, R. S. (1995). Gulf stream-generated topographic Rossby waves. *Journal of Physical Oceanography*, *25*, 574–584. https://doi.org/10.1175/1520-0485(1995)025<0574:GSTRW>2.0.CO;2

Rainville, L., Lee, C., & Woodgate, R. (2011). Impact of wind-driven mixing in the Arctic Ocean. *Oceanography*, *24*(3), 136–145. https://doi.org/10.5670/oceanog.2011.65

Rainville, L., & Woodgate, R. (2009). Observation of internal wave generation in the seasonally ice-free Arctic. *Geophysical Research Letters*, *36*, L23604. https://doi.org/10.1029/2009GL041291

Rhines, P. (1970). Edge-, bottom-, and Rossby waves in a rotating stratified fluid. *Geophysical Fluid Dynamics*, *1*(3–4), 273–302. https://doi.org/10.1080/03091927009365776

Schlichtholz, P. (2002). On a modified arrested topographic wave in Fram Strait. *Journal of Geophysical Research*, *107*(C11), 3189. https://doi.org/10.1029/2001JC000799

Shilo, E., Ashkenazy, Y., Rimmer, A., Assouline, S., Katsafados, P., & Mahrer, Y. (2007). Effect of wind variability on topographic waves: Lake Kinneret case. *Journal of Geophysical Research*, *112*, C12024. https://doi.org/10.1029/2007JC004336

Shimada, K., Itoh, M., Nishino, S., McLaughlin, F., Carmack, E., & Proshutinsky, A. (2005). Halocline structure in the Canada Basin of the Arctic Ocean. *Geophysical Research Letters*, *32*, L03605. https://doi.org/10.1029/2004GL021358

Simons, T. J. (1975). Verification of numerical models of Lake Ontario. II. Stratified circulations and temperature changes. *Journal of Physical Oceanography*, *5*, 98–110. https://doi.org/10.1175/1520-0485(1975)005<0098:vonmol>2.0.co;2

Thompson, R. O. R. Y., & Luyten, J. R. (1976). Evidence for bottom-trapped topographic Rossby waves from single moorings. *Deep Sea Research and Oceanographic Abstracts*, *23*(7), 629–635. https://doi.org/10.1016/0011-7471(76)90005-X

Timmermans, M. L., Rainville, L., Thomas, L., & Proshutinsky, A. (2010). Moored observations of bottom-intensified motions in the deep Canada Basin, Arctic Ocean. *Journal of Marine Research*, *68*(3), 625–641. https://doi.org/10.1357/002224010794657137

Torres-Valdés, S., Tsubouchi, T., Bacon, S., Naveira-Garabato, A. C., Sanders, R., McLaughlin, F. A., et al. (2013). Export of nutrients from the Arctic Ocean. *Journal of Geophysical Research: Oceans*, *118*, 1625–1644. https://doi.org/10.1002/jgrc.20063

Woodgate, R. (2013). Arctic Ocean circulation: Going around at the top of the world. *Nature Education Knowledge*, *4*(8), 8.

Woodgate, R., Aagaard, K., Swift, J. H., William, M. S. Jr., & Falkner, K. K. (2007). Atlantic water circulation over the Mendeleev Ridge and Chukchi Borderland from thermohaline intrusions and water mass properties. *Journal of Geophysical Research*, *112*, C02005. https://doi.org/10.1029/2005JC003416

Zakharchuk, E. A. (2009). Anemobaric low-frequency waves in the Chukchi Sea. *Russian Meteorology and Hydrology*, *34*(6), 371–378. https://doi.org/10.3103/S1068373909060053

Zhao, B., & Timmermans, M. (2018). Topographic Rossby waves in the Arctic Ocean's Beaufort Gyre. *Journal of Geophysical Research: Oceans*, *123*, 6521–6530. https://doi.org/10.1029/2018JC014233